Research Article | Vol. 32, No. 4 / 12 Feb 2024 / Optics Express 6076
Optics EXPRESS

Directing valley-polarized emission of 3 L WS_2 by photonic crystal with directional circular dichroism

WENZHUO HUANG,[1] CHAWINA DE-EKNAMKUL,[2] YUNDONG REN,[2] AND ERTUGRUL CUBUKCU[1,2,*]

[1]Department of Electrical and Computer Engineering, University of California, San Diego, La Jolla, California 92093-0407, USA
[2]Department of NanoEngineering, University of California, San Diego, La Jolla, California 92093-0448, USA
[*]ecubukcu@ucsd.edu

Abstract: The valley degree of freedom that results from broken inversion symmetry in two-dimensional (2D) transition-metal dichalcogenides (TMDCs) has sparked a lot of interest due to its huge potential in information processing. In this experimental work, to optically address the valley-polarized emission from three-layer (3 L) thick WS_2 at room temperature, we employ a SiN photonic crystal slab that has two sets of holes in a square lattice that supports directional circular dichroism engendered by delocalized guided mode resonances. By perturbatively breaking the inversion symmetry of the photonic crystal slab, we can simultaneously manipulate s and p components of the radiating field so that these resonances correspond to circularly polarized emission. The emission of excitons from distinct valleys is coupled into different radiative channels and hence separated in the farfield. This directional exciton emission from selective valleys provides a potential route for valley-polarized light emitters, which lays the groundwork for future valleytronic devices.

1. Introduction

In two-dimensional (2D) transition-metal dichalcogenides (TMDCs), broken inversion symmetry gives rise to a new valley degree of freedom, which has enormous implications for information processing [1,2]. The indirect bandgaps in the bulk states of TMDCs transition to energy-degenerate direct bandgaps at K and K' valleys with contrasting Berry curvatures and orbital magnetic moments when they thin down to monolayers [3–7]. Owing to the strong spin-orbit coupling at K and K' valleys, valley-polarized excitons may be optically manipulated under optical selection rules [8–13]: that is left-handed circularly polarized photons can only generate band-edge excitons at the K valley, whose emission follows the helicity of the excitation photons. This valley selective photoluminescence (PL) is critical for the development of valley-based light emitters, which will serve as the foundation for future valleytronic devices [14,15].

However, at room temperature, intervalley coupling between excitons can drastically diminish valley coherence, making valley-dependent functions difficult to implement. Although changes in the environment, such as temperature [6,9,12], external fields [16–19], or mechanical strain [20], may be used to tune valley polarization, most of them pose challenges for straightforward implementations. Few-layer TMDCs, on the other hand, offer a viable option for valleytronic devices since carrier mobility increases as the number of layers grows [21]. As a result, few-layer TMDCs have a shorter exciton lifetime and increased valley coherence [22]. To this end, here, we employ 3 L WS_2 for our valleytronic device because of its ability to maintain appreciable room temperature valley polarization.

#510027 https://doi.org/10.1364/OE.510027
Journal © 2024 Received 26 Oct 2023; revised 10 Jan 2024; accepted 19 Jan 2024; published 6 Feb 2024

Optics EXPRESS

To construct a valley-polarized emitter based on TMDCs, excitons from distinct valleys must be separated via coupling to distinct radiative modes that match their radiative character, i.e. selection rules. By integrating TMDCs with nanostructures that response differently to valley pseudo-spin, excitons from distinct valleys are coupled with different radiative channels [23–25]. Spin-momentum locked modes supported by nanowires [26,27], asymmetric grooves [28], or domain boundaries [29] have been proposed previously to segregate valley excitons, although the light-matter interaction is generally restricted to a narrow spatial region in one dimension. Alternatively, 2D photonic nanostructures with circular dichroism, such as chiral metasurfaces [30–34] and asymmetric nanoantennae [35,36], are proposed to increase the interaction volume. However, the resonances in these structures are still localized and experience high material losses, limiting propagation of exciton emission over large distances. To address these issues, we propose to integrate 3 L WS_2 with a dielectric photonic crystal (PhC) slab that supports delocalized guided mode resonances [37,38]. Photonic crystals, as a versatile platform for modifying the polarization state of radiation [39–41], have demonstrated high level of control over the emission rate and radiation pattern of dipole emitters [42–45]. Delocalized photonic Fano resonances match particularly well with the 2D TMDCs in the transverse direction [46]. In this work, the radiative channels of the PhC slab are designed in such a way that they correspond to the helicity of circular polarization and only couple with the excitons from distinct valleys. Valley-polarized exciton emission is therefore separated in the far-field as a result.

2. Concept and design

As an optical counterpart to solid state crystals, photonic crystals feature a periodic arrangement of unit cells with symmetry. Supported by the PhC slabs with finite thickness, guided mode resonances with frequency above the light cone can couple to free-space plane waves with the same in-plane momentum. This coupling is well characterized by temporal couple-mode theory [40,47], which not only predicts the Fano lineshapes of these resonances but also offers information on the polarization states of the outgoing waves. The phase difference between the out-coupling coefficients in s- (Transverse Electric (TE)) and p- (Transverse Magnetic (TM)) polarization, d_s and d_p, of a PhC slab in the x-y plane with rotational symmetry around the z-axis (C_2) is constrained by the direct (non-resonant) scattering components via

$$\arg\left(\frac{d_s}{d_p}\right) = \frac{1}{2}\arg\left(\frac{r_s + \sigma t_s}{r_p + \sigma t_p}\right) + N\pi \tag{1}$$

where r_s, t_s, r_p and t_p are the s- and p-polarized non-resonant reflection and transmission coefficients at the resonance frequency when photonic crystal slab is treated as a homogeneous dielectric slab, and $\sigma = \pm 1$ are for TE-like and TM-like resonances, respectively. Here, we only consider TE-like resonances since excitons in WS_2 are in the transverse directions, hence $\sigma = 1$ in all cases. The far-field polarization vector is represented by $\vec{d} = d_s\hat{s} + d_p\hat{p}$. To get a resonance that can couple with circularly polarized light, d_s and d_p must have comparable amplitudes and a phase difference that is close to $\pm\pi/2$. However, these two conditions are barely satisfied simultaneously for most photonic crystal slabs with C_2 symmetry. As an example, when direct scattering is on a Fabry-Pérot resonance ($t_s = t_p = \pm 1$), the phase difference between d_s and d_p would be $N\pi$, which corresponds to a linearly polarized state. Nevertheless, by breaking the in-plane inversion symmetry, two opposite propagation directions $\pm\boldsymbol{k}_\parallel$ are no longer equivalent. This means a time-reversal operation will also flip the in-plane momentum, and the out-coupling coefficients are jointly constrained by:

$$\arg\left[\frac{d_s(\boldsymbol{k}_\parallel)d_s(-\boldsymbol{k}_\parallel)}{d_p(\boldsymbol{k}_\parallel)d_p(-\boldsymbol{k}_\parallel)}\right] = \arg\left(\frac{r_s + \sigma t_s}{r_p + \sigma t_p}\right) \tag{2}$$

Optics EXPRESS

where d_s and d_p are now dependent on the in-plane momentum $\pm\boldsymbol{k}_\parallel$. Even if the right-hand side of the above equation is zero, the phase difference $\arg(d_s(\boldsymbol{k}_\parallel)/d_p(\boldsymbol{k}_\parallel))$ may still be non-zero. Specifically, when the propagation vectors are perpendicular to the mirror surface of the persisted reflection symmetry, $d_s(\boldsymbol{k}_\parallel) = -d_s(-\boldsymbol{k}_\parallel)$ and $d_p(\boldsymbol{k}_\parallel) = d_p(-\boldsymbol{k}_\parallel)$ should hold. In this situation, we get

$$\arg\left[\frac{d_s(\pm\boldsymbol{k}_\parallel)}{d_p(\pm\boldsymbol{k}_\parallel)}\right] = \frac{1}{2}\arg\left(\frac{r_s+\sigma t_s}{r_p+\sigma t_p}\right) \pm \frac{1}{2}\pi \tag{3}$$

where the extra $\pm\pi/2$ phase shift originates from the negative sign of d_s in opposite directions. As a result, the far-field polarization field can be elliptically polarized in $(\pm\boldsymbol{k}_\parallel, \boldsymbol{k}_\perp)$ directions with opposing helicity, where $\boldsymbol{k}_\perp$ denotes the out-of-plane momentum (Fig. 1(a)). An out-going wave with directional circular polarization can be achieved by tweaking the parameters of a photonic crystal, which is ideal for separating valley-polarized excitons.

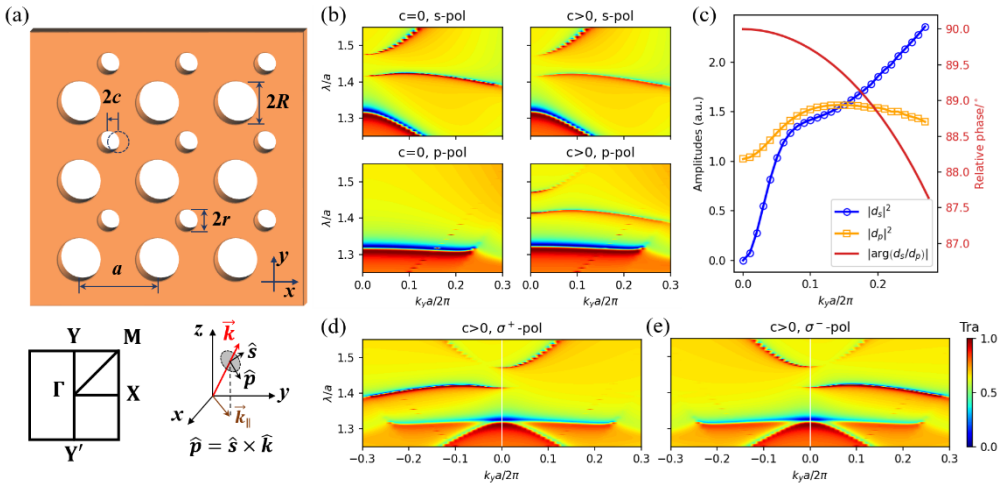

Fig. 1. (a) Breaking the inversion symmetry of a PhC slab by a perturbation. The smaller holes are shifted by $2c$ along x-axis, making Γ-Y and Γ-Y' directions inequivalent. (b) Transmission spectra of photonic bands before and after the perturbation versus k_y. A p-polarized band appears at the same location as the pre-existed s-polarized band. (c) Amplitudes and relative phase of coupling coefficients d_s and d_p versus k_y. Transmission spectra of (d) σ^+ and (e) σ^- polarized incident plane waves. The asymmetric patterns reflect directional circular dichroism in this PhC slab.

We start with a SiN photonic crystal slab that has two sets of holes in a square lattice. Each smaller hole is at the center of four neighboring larger holes, making this structure C_2 symmetric. By shifting the smaller holes by $2c$ along x direction in Fig. 1(a), the in-plane inversion symmetry is broken as the larger holes and the smaller holes are not interchangeable; nevertheless, the mirror symmetry at the x-z surface is retained. In the First Brillouin zone of this photonic crystal, Γ-Y and Γ-Y' directions that are perpendicular to the mirror surface become non-equivalent. Y(Y') points in this context are defined as $\boldsymbol{k}_\parallel = (0, \pm\pi/a)$, where a is the lattice constant. This relative shifting of the air holes, if is small compared to the lattice constant, could act as a perturbation to the lattice that splits an isolated s band into energy-degenerate s and p bands as calculated by Rigorous Couple Wave Analysis (RCWA) in Fig. 1(b). As reported in literature, we also verified that the radiative decay γ_p of generated p band at the Γ point is proportional to the square of the displacement c [48,49]. This monotonic increase of p-polarized coupling coefficient $|d_p|$ (which is equal to $\sqrt{\gamma_p}$ at the Γ point) guarantees an interception of $|d_s(\theta)|$ and $|d_p(\theta)|$ at a certain angle if the shifting length c is properly chosen. Moreover, since shifting

Optics EXPRESS

the holes will not change the effective index of the slab, the phase difference between d_s and d_p remains unchanged in equation (3). Here, the parameters of the PhC slab are as follows: refractive index n = 2.17, slab thickness t = 100 nm, lattice constant a = 440 nm, large hole radius R = 120 nm, small hole radius r = 60 nm, and displacement c = 12 nm. In Fig. 1(c), the angular dependence of the relative phase between d_s and d_p is calculated using the effective refractive index of the slab, i.e. the square root of the spatially-averaged permittivity. The amplitudes of d_s and d_p are extracted from the lineshapes of the resonances in Fig. 1(b). Within a wide range along the Γ-Y direction, where d_s and d_p have comparable amplitudesand $\sim \pi/2$ out of phase, the out-going wave would present a near circular polarization. This is verified by the RCWA simulated angle-resolved transmission spectra of a left-hand circularly polarized (σ^+) plane wave in Fig. 1(d). The large resonance amplitude in the Γ-Y' direction indicates that the resonance is σ^+ polarized, while the diminishing amplitude of resonance in the Γ-Y direction indicates a resonance with opposite helicity (σ^- polarized). If pumped with σ^- polarized plane wave, the corresponding angle-resolved spectra will be mirrored against Γ point, as shown in Fig. 1(e). In contrast, the transmission spectra of PhC slabs without shifting the holes will always present symmetric patterns against the Γ point regardless of the pump polarization due to the preserved C_2 symmetry. This reveals the unparalleled capability of a photonic crystal slab with broken inversion symmetry in controlling circular polarization in the momentum space.

To further explore the ability of our design in separating valley excitons, we place a dipole emitter at the top surface of a photonic crystal slab in FDTD simulations to mimic the experimental case of valley excitons at the near field. The PhC slab in this simulation has 20-by-20 unit-cells. The farfield radiation pattern is determined at the resonant wavelength using near-field distribution calculated slightly above the top surface of the slab. First, the dipole emitter is set to be y-polarized. The farfield intensity, given by $|E_x|^2+|E_y|^2$, is equally distributed in + y and -y directions as shown in Fig. 2(a). Because the out-going wave from this PhC slab has directional circular dichroism in Γ-Y(Y') directions, we can also extract the circularly polarized components through $E_\pm = (E_x \pm iE_y)/\sqrt{2}$ in the farfield. The farfield emission pattern of $|E_+|^2$ in Fig. 2(b) shows a stark contrast between out-going waves in $\pm k_y$ directions, which proves that these radiative

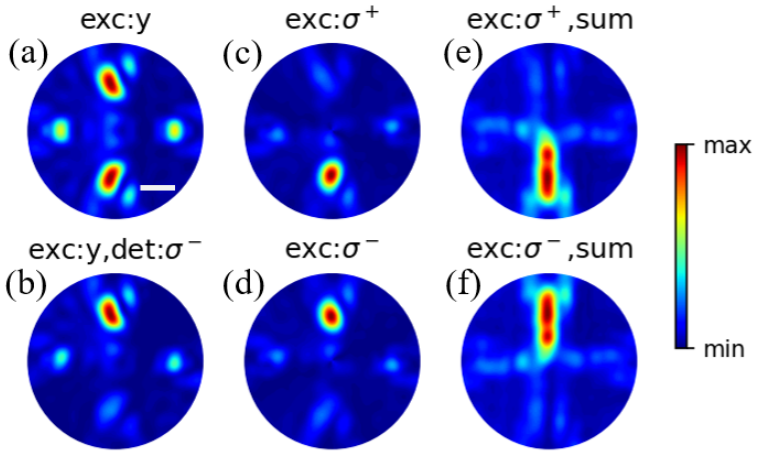

Fig. 2. Fig. 2 (a) Farfield radiation pattern from a y-polarized local dipole emitter at the resonant wavelength. The white scale bar is 0.2 NA (numerical aperture) corresponding to 11°. (b) σ^- polarized component of the farfield emission from a y-polarized dipole at the resonant wavelength. Farfield radiation patterns from a chiral emitter with (c) σ^+ and (d) σ^- polarizations at the resonant wavelength. Farfield radiation patterns from a broadband chiral emitter with (e) σ^+ and (f) σ^- polarizations.

Optics EXPRESS

channels are indeed circular polarized. Next, we create a chiral emitter by placing two orthogonal dipoles at ±90° phase difference for left or right circular polarization to emulate valley-polarized WS_2 emission. The farfield intensity $|E_x|^2+|E_y|^2$ for both polarizations are shown in Figs. 2(c) and 2(d). When excitons from one valley are selectively pumped, they tend to couple into the guided resonance that has circularly polarized farfield with same helicity. Finally, considering the broadband nature of the excitonic emission, we sum up the farfield intensities of all wavelength components near the A exciton peak of WS_2 to get a more realistic radiation pattern. In Figs. 2(e) and 2(f), these comprehensive farfield patterns from left and right circularly polarized broadband emitters exhibit an emission strip along $\mp k_y$ directions, respectively.

3. Experimental results and discussion

To experimentally observe the directional circular dichroism in a photonic crystal slab with broken inversion symmetry, we fabricated SiN photonic crystal slabs with the proposed parameters using electron beam lithography. We then measured the angle-resolved transmission spectra of the PhC slab by putting the sample on a rotational stage illuminated by collimated white light. Here, we chose a PhC sample with a slightly larger displacement (c = 20 nm) than that in the simulation for larger angular separation in the farfield. In Figs. 3(a) and 3(b), measured angle-resolved transmission spectra for s- and p- polarizations in both Γ-Y and Γ-Y' directions are shown. These spectra are symmetric with respect to the Γ point. We then measured σ^+ and σ^- polarized transmission spectra and the results are shown in Figs. 3(c) and 3(d). Here, the transmission spectra demonstrate an asymmetric pattern in $\pm k_y$ directions as a result of broken inversion symmetry in the PhC slab. This directional coupling of circularly polarized resonance agrees well with our simulation, showing its promising ability in controlling the radiation pattern with helicity.

We then transferred a mechanically exfoliated 3 L WS_2 onto the PhC slab. The optical image of the WS_2/PhC sample is shown in Fig. 4(a). The sample was excited by a linearly polarized 594 nm laser through a 0.9 NA objective, and the PL was collected through a polarizer for co- and cross-polarized spectra, respectively (Fig. 4(b)). The degree of valley polarization at the A exciton resonance is around 30%~40%. This is slightly lower than a suspended 3 L WS_2 due to the PL from the SiN PhC slab itself that cannot be completely removed by subtraction. We expect the valley polarization to depend on the quantum yield, which is affected by the SiN substrate as well. Another peak ~ 780 nm is due to the indirect bandgap emission of 3 L WS_2 [50], which has zero valley polarization as expected. The peaks around 608 nm are Raman peaks from phonon modes in WS_2.

To verify the ability of the PhC slab in modifying the farfield polarization, we performed polarization resolved PL imaging of the back focal plane of the objective corresponding to the momentum space. With a laser polarized linearly in y direction, excitons from K and K' valleys are equally stimulated. Using a quarter waveplate and a linear polarizer on the detection side, σ+ and σ− polarized components of PL can be resolved and separated in the farfield. In Figs. 4(c) and 4(d), angle-resolved PL with $k_x = 0$ and k_y ranging from -0.5k_0 to 0.5k_0 were measured with σ+ and σ− detectors, where $k_0 = 2\pi/\lambda$ is the free-space photon momentum. The spatial dispersion of PL corresponds to the band structure of the PhC slab, which is consistent with the asymmetric transmission spectra. A redshift in resonance wavelength was observed due to the addition of 3 L WS_2, whose real part of the refractive index is around 5 in the visible range, increasing the effective mode index. This measurement confirms that the directional emission from the radiative channels are circularly polarized, and their helicity is correlated to the momentum in y direction. The degree of circular polarization, as calculated by $(I_{\sigma^+} - I_{\sigma^-})/(I_{\sigma^+} + I_{\sigma^-})$, reaches up to 66% within PL wavelengths. In addition to the angle-resolved spectra, we also imaged the farfield radiation pattern from the back focal plane. A 650 nm low-pass filter was used to remove the indirect bandgap emission. The pump laser at 594 nm was still y-polarized. As

Optics EXPRESS

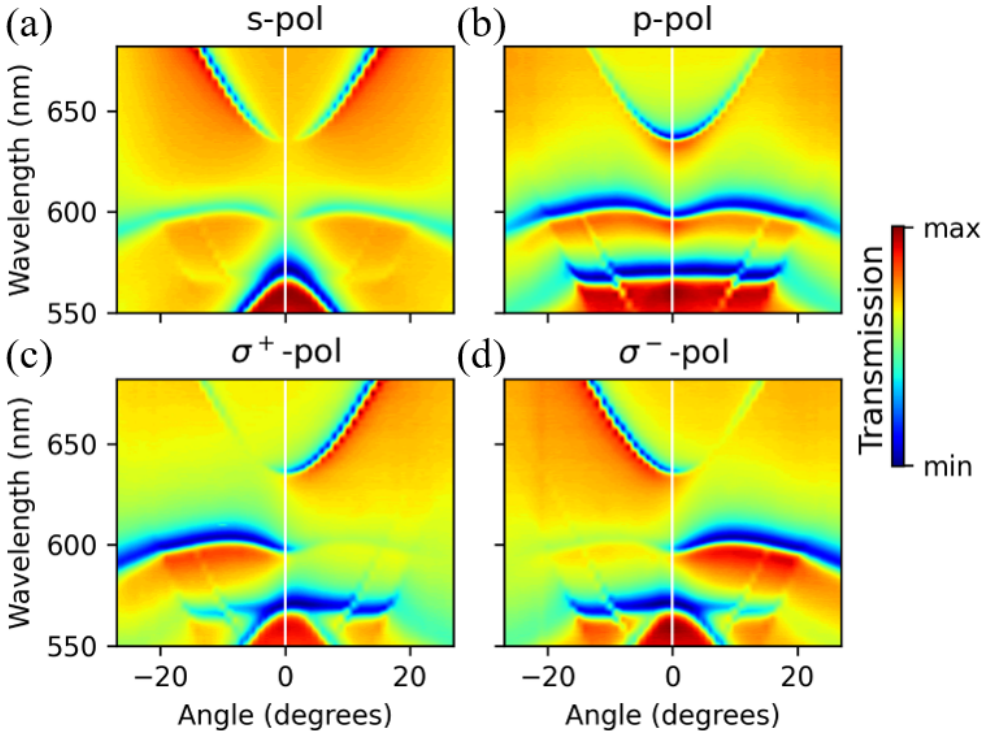

Fig. 3. Experimental angle-resolved transmission spectra of the PhC slab with broken inversion symmetry. The measurement is along Y'-Γ-Y direction. The spectra are symmetric against Γ point for (a) s- and (b) p-polarizations due to the mirror symmetry by the xz plane; but they are asymmetric for (c) σ^+ and (d) σ^- polarizations because of the opposite helicity of the supported circularly polarized states in Γ-Y and Γ-Y' directions.

shown in Figs. 4(e-g), back focal plane images with y, σ+ and σ− polarized components were taken. Clearly, these images show that the exciton emission from 3 L WS_2 is separated in the farfield corresponding to the helicity of their circular polarization: left (right) handed circularly polarized component is mainly directed to the free-space with a negative (positive) momentum in y direction.

Furthermore, owing to polarization dependent valley excitonic emission in 3 L WS_2, the farfield pattern from our WS_2/PhC device could be solely modulated by the polarization state of the pump. In Figs. 5(a-d), the polarization states of the pump laser were set to be x, y, σ^+ and σ^-, respectively; and there was no polarizer on the detection side. To remove the Raman features, the PL is filtered through a 10 nm band pass filter centered at 630 nm. When the pump laser was linearly polarized, excitons from both valleys are generated equally. Thus, the farfield pattern is symmetric in $\pm k_y$ directions as shown in Figs. 5(a) and 5(b). When the pump laser was circularly polarized, however, excitons from one valley are generated more efficiently than the other one due to the selection rules. This selective excitation of valley excitons leads to imbalanced circularly polarized components in the exciton emission. As circular polarization states with opposite helicity are separated in the momentum space by different radiative channels supported by the PhC slab, asymmetric farfield patterns are observed with circularly polarized pump in Figs. 5(c) and 5(d). Here, the degree of circular polarization is determined not only by the circular polarization of the radiative channels, but also by the valley polarization of the 3 L WS_2. Their product determines the upper limit of the degree of circular polarization with

Optics EXPRESS

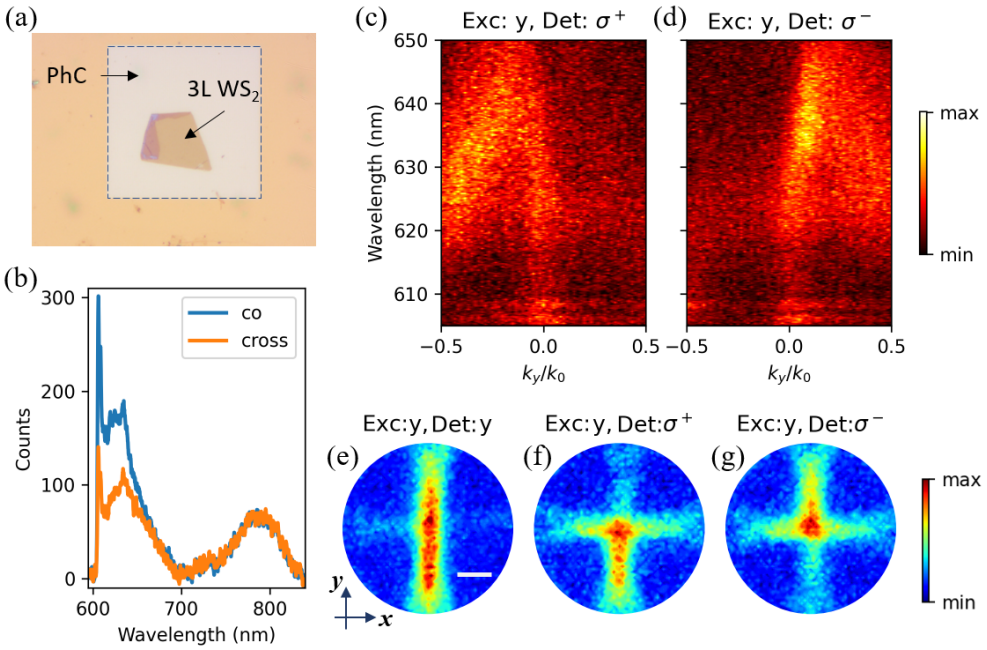

Fig. 4. (a) Optical image of the 3 L WS_2/PhC sample. The fabricated PhC consisting of 100×100 unit-cells is outlined with the dashed square (w = 44 µm). (b) Polarization resolved PL spectra of the 3 L WS_2 on PhC. (c) σ^+ and (d) σ^- polarized components of PL spectra versus k_y. The sample is excited by a linearly polarized laser in y direction. Farfield radiation patterns of (e) y, (f) σ^+ and (g) σ^- polarized components. The scale bar is 0.2 NA (11°).

a selective circularly polarized pump, assuming perfect coupling between circularly polarized emission and the polarization-dependent radiative channels. In this device, the limit is calculated to be 23% from previous results, and we experimentally observed a circular polarization of around 8%. This proof-of-concept experiment demonstrates that a PhC slab with directional circular dichroism may be utilized to distinguish farfield emission of different circular helicities originating from valley-polarized excitons. We argue that the degree of separation can be further improved by both enhancing valley polarization of the light emitter, which is achievable through cooling to cryogenic temperatures or employing materials with higher valley coherence [51], and increasing the circular dichroism of the PhC slab by optimizing its geometry.

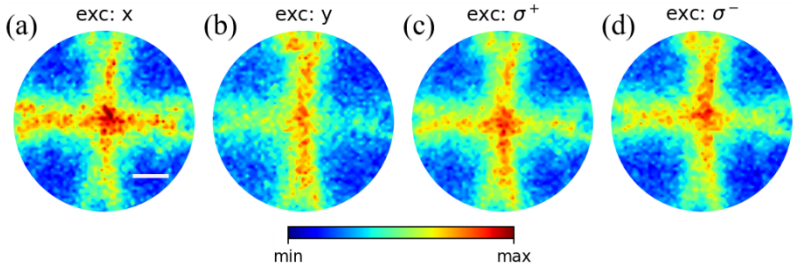

Fig. 5. Farfield radiation patterns with (a) x, (b) y, (c) σ^+ and (d) σ^- polarized pump laser. The scale bar is 0.2 NA (11°). The PL is filtered by a 10 nm band pass filter centered at 630 nm. Valley-polarized exciton emission is coupled into different radiative channels depending on the polarization.

Optics EXPRESS

In summary, we experimentally demonstrated a PhC slab design exhibiting directional circular dichroism for separating valley-polarized exciton emission from a 3 L WS_2 in the farfield. A perturbation is introduced to the PhC slab such that it breaks the in-plane inversion symmetry and creates directional circularly polarized radiative channels with opposite helicity. This allows us to either separate the valley coherent excitonic emission on the detection side, or to selectively pump excitons from one valley to generate an asymmetric radiation pattern. Owing to its ability to direct exciton emission from distinct valleys into different directions, this design offers an ideal platform for future valley-coherent optoelectronics.

Funding. National Science Foundation (ECCS-2139416); National Eye Institute (1R21EY033676).

Acknowledgments. This work was supported by NSF under the NSF EAGER-Program (ECCS-2139416) and National Institutes of Health, National Eye Institute (1R21EY033676). This work was performed in part at the San Diego Nanotechnology Infrastructure (SDNI) at the University of California, San Diego (UCSD), a member of the National Nanotechnology Coordinated Infrastructure (NNCI), which is supported by the National Science Foundation (ECCS-1542148).

Disclosures. The authors declare no conflicts of interest.

Data availability. Data underlying the results presented in this paper are not publicly available at this time but may be obtained from the authors upon reasonable request.

References

1. T. Cao, G. Wang, W. Han, *et al.*, "Valley-selective circular dichroism of monolayer molybdenum disulphide," Nat. Commun. **3**(1), 887 (2012).
2. R. Suzuki, M. Sakano, Y. J. Zhang, *et al.*, "Valley-dependent spin polarization in bulk MoS_2 with broken inversion symmetry," Nat. Nanotechnol. **9**(8), 611–617 (2014).
3. W. Zhao, R. M. Ribeiro, M. Toh, *et al.*, "Origin of indirect optical transitions in few-layer MoS_2, WS_2, and WSe_2," Nano Lett. **13**(11), 5627–5634 (2013).
4. H. Zeng, G. B. Liu, J. Dai, *et al.*, "Optical signature of symmetry variations and spin-valley coupling in atomically thin tungsten dichalcogenides," Sci. Rep. **3**(1), 1608 (2013).
5. X. Xu, W. Yao, D. Xiao, *et al.*, "Spin and pseudospins in layered transition metal dichalcogenides," Nat. Phys. **10**(5), 343–350 (2014).
6. B. Zhu, H. Zeng, J. Dai, *et al.*, "Anomalously robust valley polarization and valley coherence in bilayer WS_2," Proc. Natl. Acad. Sci. U. S. A. **111**(32), 11606–11611 (2014).
7. C. Mai, Y. G. Semenov, A. Barrette, *et al.*, "Exciton valley relaxation in a single layer of WS2 measured by ultrafast spectroscopy," Phys. Rev. B: Condens. Matter Mater. Phys. **90**(4), 041414 (2014).
8. K. F. Mak, K. He, J. Shan, *et al.*, "Control of valley polarization in monolayer MoS_2 by optical helicity," Nat. Nanotechnol. **7**(8), 494–498 (2012).
9. H. Zeng, J. Dai, W. Yao, *et al.*, "Valley polarization in MoS_2 monolayers by optical pumping," Nat. Nanotechnol. **7**(8), 490–493 (2012).
10. A. M. Jones, H. Yu, N. J. Ghimire, *et al.*, "Optical generation of excitonic valley coherence in monolayer WSe_2," Nat. Nanotechnol. **8**(9), 634–638 (2013).
11. Z. Ye, D. Sun, and T. F. Heinz, "Optical manipulation of valley pseudospin," Nat. Phys. **13**(1), 26–29 (2017).
12. Y.-J. Chen, J. D. Cain, T. K. Stanev, *et al.*, "Valley-polarized exciton–polaritons in a monolayer semiconductor," Nat. Photonics **11**(7), 431–435 (2017).
13. S. Dufferwiel, T. P. Lyons, D. D. Solnyshkov, *et al.*, "Valley coherent exciton-polaritons in a monolayer semiconductor," Nat. Commun. **9**(1), 4797 (2018).
14. T. Mueller and E. Malic, "Exciton physics and device application of two-dimensional transition metal dichalcogenide semiconductors," *npj 2D Materials and Applications 2* (2018).
15. Y. Liu, Y. Gao, S. Zhang, *et al.*, "Valleytronics in transition metal dichalcogenides materials," Nano Res. **12**(11), 2695–2711 (2019).
16. Y. J. Zhang, T. Oka, R. Suzuki, *et al.*, "Electrically switchable chiral light-emitting transistor," Science **344**(6185), 725–728 (2014).
17. C. Chakraborty, A. Mukherjee, L. Qiu, *et al.*, "Electrically tunable valley polarization and valley coherence in monolayer WSe2 embedded in a van der Waals heterostructure," Opt. Mater. Express **9**(3), 1479–1487 (2019).
18. C. Rupprecht, E. Sedov, M. Klaas, *et al.*, "Manipulation of room-temperature valley-coherent exciton-polaritons in atomically thin crystals by real and artificial magnetic fields," 2d Mater 7 (2020).
19. R. Shreiner, K. Hao, A. Butcher, *et al.*, "Electrically controllable chirality in a nanophotonic interface with a two-dimensional semiconductor," Nat. Photonics **16**(4), 330–336 (2022).
20. C. R. Zhu, G. Wang, B. L. Liu, *et al.*, "Strain tuning of optical emission energy and polarization in monolayer and bilayer MoS2," Phys. Rev. B: Condens. Matter Mater. Phys. **88**(12), 121301 (2013).

Optics EXPRESS

21. S. L. Li, K. Tsukagoshi, E. Orgiu, *et al.*, "Charge transport and mobility engineering in two-dimensional transition metal chalcogenide semiconductors," Chem. Soc. Rev. **45**(1), 118–151 (2016).
22. L. Yuan and L. Huang, "Exciton dynamics and annihilation in WS_2 2D semiconductors," Nanoscale **7**(16), 7402–7408 (2015).
23. A. Krasnok and A. Alù, "Valley-Selective Response of Nanostructures Coupled to 2D Transition-Metal Dichalcogenides," Appl. Sci. **8**(7), 1157 (2018).
24. R. Peng, C. Wu, H. Li, *et al.*, "Separation of the valley exciton-polariton in two-dimensional semiconductors with an anisotropic photonic crystal," Phys. Rev. B **101**(24), 245418 (2020).
25. S. Li, H. Wang, J. Wang, *et al.*, "Control of light-valley interactions in 2D transition metal dichalcogenides with nanophotonic structures," Nanoscale **13**(13), 6357–6372 (2021).
26. S.-H. Gong, F. Alpeggiani, B. Sciacca, *et al.*, "Nanoscale chiral valley-photon interface through optical spin-orbit coupling," Science **359**(6374), 443–447 (2018).
27. P. G. Chen, Z. Li, Y. Qi, *et al.*, "Long-Range Directional Routing and Spatial Selection of High-Spin-Purity Valley Trion Emission in Monolayer WS_2," ACS Nano **15**(11), 18163–18171 (2021).
28. L. Sun, C.-Y. Wang, A. Krasnok, *et al.*, "Separation of valley excitons in a MoS_2 monolayer using a subwavelength asymmetric groove array," Nat. Photonics **13**(3), 180–184 (2019).
29. W. Liu, Z. Ji, Y. Wang, *et al.*, "Generation of helical topological exciton-polaritons," Science **370**(6516), 600–604 (2020).
30. Z. Li, C. Liu, X. Rong, *et al.*, "Tailoring MoS_2 Valley-Polarized Photoluminescence with Super Chiral Near-Field," Adv. Mater. (Weinheim, Ger.) **30**(34), e1801908 (2018).
31. T. Chervy, S. Azzini, E. Lorchat, *et al.*, "Room Temperature Chiral Coupling of Valley Excitons with Spin-Momentum Locked Surface Plasmons," ACS Photonics **5**(4), 1281–1287 (2018).
32. G. Hu, X. Hong, K. Wang, *et al.*, "Coherent steering of nonlinear chiral valley photons with a synthetic Au–WS_2 metasurface," Nat. Photonics **13**(7), 467–472 (2019).
33. S. Guddala, R. Bushati, M. Li, *et al.*, "Valley selective optical control of excitons in 2D semiconductors using a chiral metasurface [Invited]," Opt. Mater. Express **9**(2), 536–543 (2019).
34. B. Tang, Z. Li, E. Palacios, *et al.*, "Chiral-Selective Plasmonic Metasurface Absorbers Operating at Visible Frequencies," IEEE Photon. Technol. Lett. **29**(3), 295–298 (2017).
35. H. Chen, M. Liu, L. Xu, *et al.*, "Valley-selective directional emission from a transition-metal dichalcogenide monolayer mediated by a plasmonic nanoantenna," Beilstein J. Nanotechnol. **9**, 780–788 (2018).
36. H. T. Lin, C. Y. Chang, P. J. Cheng, *et al.*, "Circular Dichroism Control of Tungsten Diselenide (WSe_2) Atomic Layers with Plasmonic Metamolecules," ACS Appl. Mater. Interfaces **10**(18), 15996–16004 (2018).
37. X. Zhang, N. Biekert, S. Choi, *et al.*, "Dynamic Photochemical and Optoelectronic Control of Photonic Fano Resonances via Monolayer MoS_2 Trions," Nano Lett. **18**(2), 957–963 (2018).
38. W. Huang, C. De-Eknamkul, X. Zhang, *et al.*, "Monolayer Excitonic Emission for Imaging Spatial Dispersion of Photonic Crystals," ACS Photonics **6**(9), 2312–2319 (2019).
39. S. Fan and J. D. Joannopoulos, "Analysis of guided resonances in photonic crystal slabs," Phys. Rev. B **65**(23), 235112 (2002).
40. B. Z. Chia Wei Hsu, Marin Soljačić, and A. Douglas Stone, "Polarization state of radiation from a photonic crystal slab," (2017).
41. W. Liu, B. Wang, Y. Zhang, *et al.*, "Circularly Polarized States Spawning from Bound States in the Continuum," Phys. Rev. Lett. **123**(11), 116104 (2019).
42. B. Zhen, S. L. Chua, J. Lee, *et al.*, "Enabling enhanced emission and low-threshold lasing of organic molecules using special Fano resonances of macroscopic photonic crystals," Proc. Natl. Acad. Sci. U. S. A. **110**(34), 13711–13716 (2013).
43. S. V. Lobanov, S. G. Tikhodeev, N. A. Gippius, *et al.*, "Controlling circular polarization of light emitted by quantum dots using chiral photonic crystal slabs," Phys. Rev. B: Condens. Matter Mater. Phys. **92**(20), 205309 (2015).
44. L. Zhang, R. Gogna, W. Burg, *et al.*, "Photonic-crystal exciton-polaritons in monolayer semiconductors," Nat. Commun. **9**(1), 713 (2018).
45. J. Wang, H. Li, Y. Ma, *et al.*, "Routing valley exciton emission of a WS_2 monolayer via delocalized Bloch modes of in-plane inversion-symmetry-broken photonic crystal slabs," Light: Sci. Appl. **9**(1), 148 (2020).
46. X. Zhang, S. Choi, D. Wang, *et al.*, "Unidirectional Doubly Enhanced MoS_2 Emission via Photonic Fano Resonances," Nano Lett. **17**(11), 6715–6720 (2017).
47. S. Fan, W. Suh, and J. D. Joannopoulos, "Temporal coupled-mode theory for the Fano resonance in optical resonators," J. Opt. Soc. Am. A **20**(3), 569–572 (2003).
48. K. Koshelev, S. Lepeshov, M. Liu, *et al.*, "Asymmetric Metasurfaces with High-Q Resonances Governed by Bound States in the Continuum," Phys. Rev. Lett. **121**(19), 193903 (2018).
49. M. Liu and D. Y. Choi, "Extreme Huygens' Metasurfaces Based on Quasi-Bound States in the Continuum," Nano Lett. **18**(12), 8062–8069 (2018).
50. A. Berkdemir, H. R. Gutiérrez, A. R. Botello-Méndez, *et al.*, "Identification of individual and few layers of WS2 using Raman Spectroscopy," Sci. Rep. **3**(1), 1755 (2013).
51. L. Du, J. Tang, J. Liang, *et al.*, "Giant Valley Coherence at Room Temperature in 3R WS_2 with Broken Inversion Symmetry," Research (Washington, DC, U. S.) **2019**, 6494565 (2019).